LARGE-SCALE TURBULENCE GENERATION AND MICROBREAKING WAVES

Ira Leifer, Brian D. Piorek, Walter C. Smith, Sanjoy Banerjee
Chemical Engineering Department
University of California,
Santa Barbara, California 93106 USA
ira.leifer@bubbleology.com,brian@piorek.net,wcsmith@engineering.ucsb.edu
banerjee@chemengr.ucsb.edu

ABSTRACT

Observations in a wind-wave channel show that microbreaking waves are distinguished by the generation of large and persistent turbulence bursts, a shear layer, a convergence zone in front of the crest and a divergence region behind the crest. Burst persistence was measured at different wind speeds, 1.5 and 2.5 m s^{-1}. The lower wind speed gives rise to occasional microbreaking, which was far more frequent at the higher wind speed. The results show that microbreaking causes a change in the burst persistence probability distribution. For the lower wind speed, persistence decreased monotonically, while at higher wind speeds it was bimodal with an additional peak at 0.25 s. This suggests a qualitative change in turbulence structure in the subsurface region caused by microbreaking.

INTRODUCTION

Microbreaking – wind-generated, short-waves breaking without air entrainment (Banner and Philips, 1974) - is observed to occur at relatively low wind speed velocities with a wavelength ~O(10 cm) and amplitude ~O(1 cm).

As microbreaking commences at wind speeds of ~3-4 m s^{-1}, it may be quite widespread since the average windspeed over the open ocean is ~7.5 m s^{-1}. Therefore microbreaking potentially affects air-water gas transfer processes and near surface mixing significantly. In support of this the Liss and Merlivat (1986) correlation of air-sea gas transfer with the 10-m wind speed, u_{10}, shows a sharp increase at u_{10} ~ 3.5 m s^{-1}, where microbreaking is thought to start.

Laboratory wind-wave channel experiments show that microbreaking is associated with a rapidly moving surface layer that travels downwind with the wave crest. Flow visualization also indicates the production of large-scale, subsurface turbulence structures. Such large bursts only are observed with microbreaking and are significantly different from those generated by wind stress at lower speeds. We start with a presentation of the phenomena in this section, and then in greater detail later. The phenomena are illustrated in Fig. 1, which shows side views of microbubble lines that acted as flow tracers for wind speeds, u_a, of 1.5 and 2.5 m s^{-1}. Figs. 1A & 1B show the formation of a normal burst. The burst formed at x = 1 cm, z = 1 cm, where x is horizontal position and z is depth and was advected to x = 3, z = 1 cm 0.8 s later (Fig. 1B). By 0.4 s it had already ceased growing.

Such bursts were first observed by Rashidi and Banerjee (1990) for wind stress without microbreaking. Under microbreaking conditions, giant bursts are observed in addition to the "normal" ones, an example of a giant burst is shown in Figs. 1C & 1D for 2.5 m s^{-1}. In Fig. 1C the burst occupies the upper left half of the image, in Fig. 1D most of the burst is off-screen, and the burst occupies the image for x < 3.5 cm, extending across the field of view. These large-scale structures give rise to upwelling and downdrafts with high surface divergence and convergence, respectively. They may significantly enhance scalar transfer at the

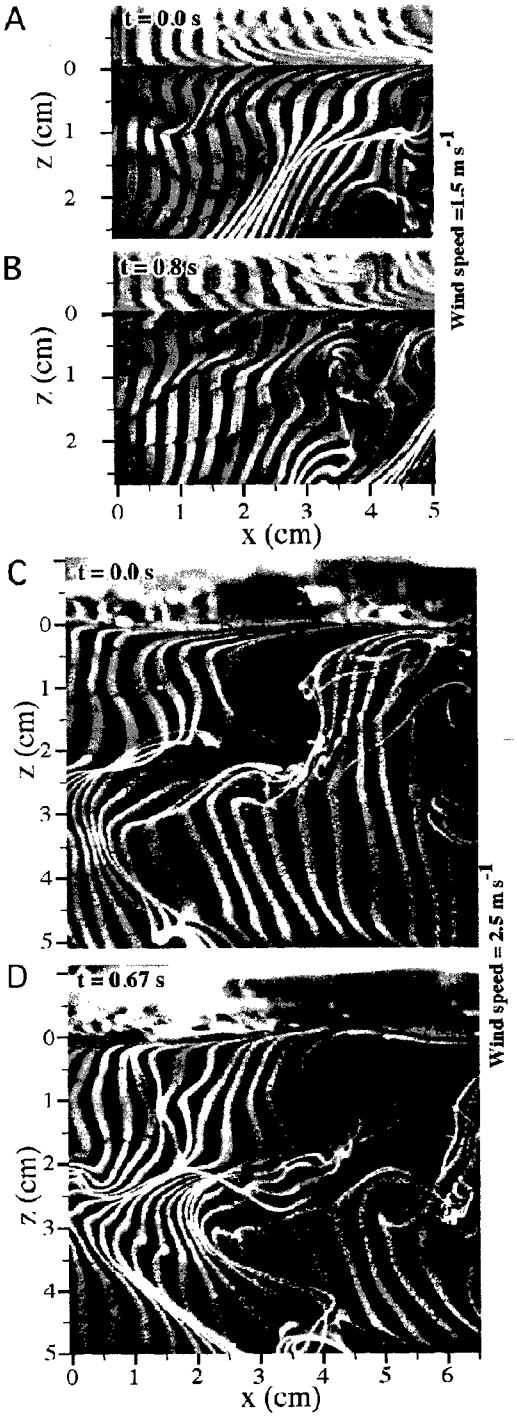

Figure 1: Side view images of normal burst (A-B) and giant burst (C-D). Horizontal, x, and depth, z, position and time, t, on figure, Wind and current are to the left. Above the interface, the image contrast was decreased.

air-sea interface compared to non-breaking conditions as mean transfer rates have been found to increase with increased surface divergence (Banerjee, 1990). Burst interactions are common at 2.5 m s^{-1} and an example is shown in Fig. 1D where a second burst enters the field of view at x = 5, z = 1.5 cm that then interacts with the giant burst. The normal wind-stress generated bursts maintain their coherence to depths of ~100-200 shear based units, whereas the giant bursts associated with microbreaking reach right to the channel bottom, ~400 shear based units.

METHODOLOGY

Lab experiments were conducted in a 0.4 x 0.9 x 12 m stainless steel channel with a 2-m long glass viewing area 6 m from the channel entry. Water and airflow depths were typically 10 and 30 cm, respectively. The large width:depth ratio reduced wall effects. Water entered the channel from a 2-m^3 holding tank through a porous filter, and exited over a gently sloped weir falling into a 2-m^3 collection tank. Thus the channel and end tanks were hydraulically isolated. A reversible variable speed fan created the wind flow while a pump generated a co-wind or counter-wind current. Water was filtered and UV sterilized continuously. An anemometer measured the wind speed in the center of the channel air space.

Liquid-side motions were visualized by using lines of oxygen microbubbles 20-50 μm in diameter generated by electrochemical pulses. The microbubble lines acted as flow tracers. Pulse width and separation were varied depending upon the wind speed. Illumination was by a vertical light sheet created with a 2° dispersion 1000W floodlight and focusing optics. In some situations, neutrally buoyant 200-μm diameter polystyrene microspheres were added to the channel. A high speed digital video camera collected images at 125 frames per second for analysis. The camera was aimed slightly upwards from the channel side, or downwards from overhead.

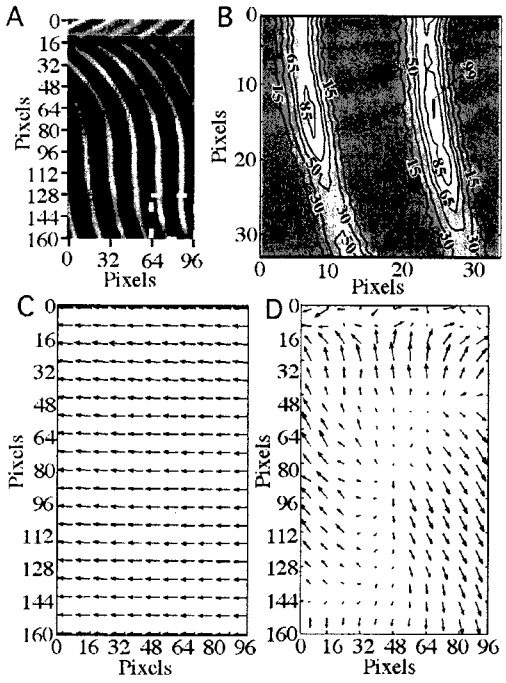

Figure 2: Image of microbubble line flow tracers (A) and intensity contours of a 32 pixel square window (B) indicated on (A) by dashed rectangle. Normalized intensity contours labeled.

Image sequences were analyzed by hierarchical digital line imaging velocimetry (HDLIV). This method is a modification of HDPIV (using particles) as described in Kumar and Banerjee (1998). Velocities are determined from cross correlations between image subsets (windows) in adjacent frames. The hierarchical approach first calculates velocities from large windows, and then used these velocities for improved positioning of smaller windows on subsequent passes. Thus HDPIV improves accuracy and allows determination of both large and small scale velocities. Both methods track image structures (particles or lines) to determine the velocity. While DPIV can use thresholded (1 bit) images, HDLIV requires 8 bit images to preserve the image structures described by intensity variations along the lines.

The approach of HDLIV is illustrated in Fig. 2. Fig. 2A shows an image section, where the contrast above the interface was decreased. Wind speed was 1 m s^{-1}. Intensity structures along the lines are shown in Fig. 2B by intensity contours for the 32x32 pixel window indicated in Fig. 2A. The calculated velocity field for Fig. 2A is shown in Fig. 2C. Velocity fluctuations were calculated by removing the mean horizontal velocity, u(z), and are shown in Fig. 2D.

DLIV has advantages and disadvantages compared to DPIV. Bubble lines have the problem that divergence and advection can remove all structures from a portion of the image, while particles in the light sheet are continually refreshed. However, to prevent particles at two different distances having different velocities, thin light sheets are required. Thus erroneous vectors arise when particles leave and enter the light sheet. DLIV instead allows thick light sheets and only suffers when lines wrap around themselves. For both approaches, the final window size must be large enough to contain image structures that can be tracked. One of DLIV's main advantages is that it can be used in conjunction with the type of flow visualization shown in Fig. 1 that aids interpretation of velocity fields.

RESULTS

Oceanic microbreaking is thought to begin at u_{10} ~3 - 4 m s^{-1}, which corresponds to a gas-side, total shear velocity, u^*_w, of ~0.3 cm s^{-1} (Coantic, 1986). We identified microbreaking waves by two mechanisms, the generation of large and persistent bursts, and by the downwind transport of surface fluid. The latter is visualized by scattering particles on the water surface. With microbreaking, the particles accumulate at the wave crests and are transported downwind with the wind waves. This surface transport is associated with strong surface divergence and convergence, as mentioned earlier.

A side-view of a giant burst using microsphere flow tracers is shown in Fig. 3A along with the calculated vorticity field (Fig. 3B). The image and vorticity shown in the figure are for ~0.2 s after burst formation. The turbulence patch remained coherent for several

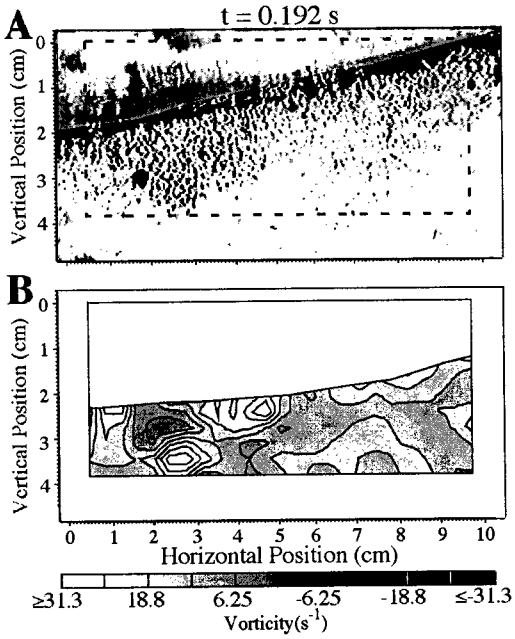

Figure 3: Side view image of a giant burst (A) and the calculated vorticity field. Dashed line on (A) shows edge of vorticity calculation region. Size and vorticity scales on figure.

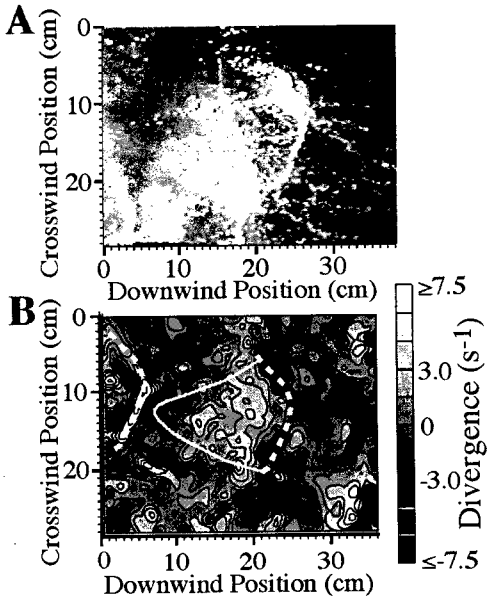

Figure 4: Top view image of a microbreaking wave (A) and the calculated divergence field. Dashed white line shows wave crest, solid white line shows extent of region of high divergence. Size and divergence scales on figure.

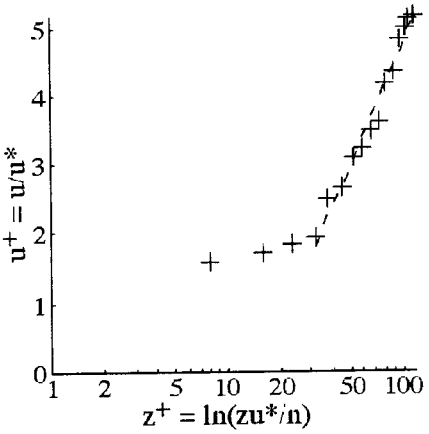

Figure 5: Liquid-side, dimensionless velocity profile, u+, versus dimensionless distance, z+, for wind speed of 2.5 m s^{-1}.

wave periods and was associated with strong periods of upwelling flow. These upwelling flows correspond to the region of strong divergence behind the microbreaking wave crest as discussed below.

An example of a microbreaking wave is shown in Fig. 4A looking downward at floating microparticle flow tracers. Horizontal velocity components were calculated by HDPIV and the estimated velocity divergence field is shown in Fig. 4B. The region behind the microbreaking wave shows a large divergence indicating an upwelling flow, while the wave crest region shows strong convergence of the flow. In the absence of microbreaking, such convergence and divergence zones are not associated with waves. The particles just bob up and down as the waves pass by.

At a mean air speed, u_a, of ~1.25 m s^{-1} in the wind-wave channel microbreaking was observed very infrequently, while for $u_a \sim 3.5$ m s^{-1} (a case not discussed here), microbreaking was common. To investigate the effect of increasing wind stress on microbreaking, the probability distribution of burst persistence was determined by HDLIV at two wind speeds, 1.5 and 2.5 m s^{-1}. Bursts were identified from both image sequences and the dimensionless liquid-side, time-varying Reynolds stress,

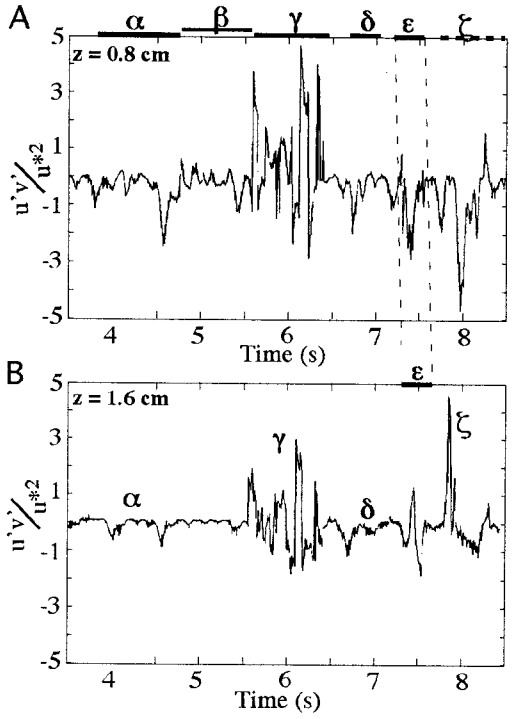

Figure 6: Time series of non-dimensional Reynolds stress ($u'v'/u^{*2}$) for wind speed, u_a = 2.5 m s^{-1} at depths of 1.2 (A) and 1.8 cm (B). Data key: Solid bar indicates bursts that originated at the air-water interface, dashed bar at the bottom, and thin bar for shear layer perturbation.

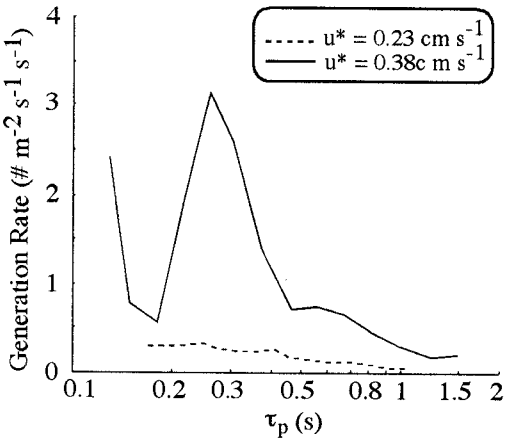

Figure 7: Burst persistence, τ_p distribution for u* = 0.23 and 0.38 cm s^{-1}. See text for details.

$u'v'/u^{*2}$, where u' and v' are the horizontal and vertical velocity fluctuations, respectively. The mean vertical horizontal velocity profile, u(z) on the liquid side was calculated from the time series to determine u'. u* was calculated from a log profile for either rough or smooth pipe flow (Bird et al., 1960) depending upon u_a, and was 0.23 and 0.38 cm s^{-1} for u_a = 1.5 and 2.5 m s^{-1}, respectively. The dimensionless velocity profile, u/u*, for u_a = 2.5 m s^{-1} is shown in Fig. 5.

Bursts were identified and counted based on the image sequences and Reynolds stress time series at several depths. The image sequences identified which periods of increased Reynolds stress were due to bursts originating at the surface and within the field of view. Surface bursts originating outside the field of view or rising from below were not counted. Visualization also allowed identification of individual bursts that coalesced in the field of view whereas examination of the Reynolds Stress record would suggest a single large burst for such events (e.g., see Fig. 1D). For each burst, the persistence time, τ_p, was recorded. The method is illustrated in Fig. 6 for a 5 second subset of the non-dimensional Reynolds stress at z = 0.8, Fig. 6A, and 1.6 cm, Fig 6B. Several bursts including a giant burst (γ) were observed primarily descending from the surface. A comparison of the Reynolds stress at the two depths shows that burst ε arrived at 1.6 cm depth 0.2s later than at 0.8 cm. In contrast, the upward rising burst ζ, arrived ~0.2 s later at the shallower depth. Thus burst origin often can be inferred from the arrival time at different depths. However this is not always the case, such as for the large burst at 5.5 s at both depths. Also shown in Fig. 6A is turbulence (β) created by the passing of the shear layer associated with the giant burst γ. These small fluctuations were associated with the shear layer and were not counted as bursts in the analysis.

The two τ_p series were histogrammed with logarithmically spaced τ_p bins (units are seconds). Distributions were normalized to per unit surface area (i.e., depth of field multiplied by the interface that passed the camera during the measurement period), per second of burst persistence, and per second (i.e., measurement

time). The τ_p distributions are shown in Fig. 7 and are the generation rate per second of bursts with different persistence times per square meter of surface area. At the lower wind speed, the generation rate decreased monotonically with τ_p and for the largest burst observed τ_p was 1.1 s. At the higher wind speed, the distribution's characteristics are very different, exhibiting a peak at 0.25 s that is qualitatively different from what is observed at the lower wind speed, and is comparable to the dominant wave period (~5 hz). For τ_p larger than the peak, the distribution decreases monotonically. Thus with the onset of microbreaking, the distribution became bimodal.

DISCUSSION AND CONCLUSION

The surface velocity field shows there is a region of convergence at the crest of microbreaking waves, which must be associated with downdrafts. Behind the crest is an area of strong divergence that is related to strong upwelling flows. The resulting flow pattern between the downdraft and the upwelling may affect burst persistence leading to the peak at τ_p = 0.25 that is about half the wave period. Giant bursts or plunging motions originate slightly behind the crest, penetrating to the channel bottom. These are accompanied by strong upwelling fluid motions, like sweeps. Furthermore, these large scale motions persist for several wave periods. Therefore they appear to be a consequence of several bursts of the type that produce the τ_p peak at 0.25 s.

In conjunction with the laboratory studies, field observations of microbreaking in the Santa Barbara Channel (10 km from shore, water depth of 600 m) have been conducted and show similarities. Suffice it to say that the regions of surface divergence and upwelling flows observed behind the laboratory microbreaking waves are also evident in the field measurements and the wavelengths and amplitudes are similar.

ACKNOWLEDGMENTS

This work has been performed with the support of the Department of Energy, Grant No. DE-F603-85ER-13314.

REFERENCES

Banerjee, S., 1990, "Turbulence Structure and Transport Mechanisms at Interfaces" Keynote Lecture, 9th Int. Heat Transfer Conf, Hemisphere Press, NY, pp. 395-418.

Bird, R.B., W.E. Stewart, and E.N. Lightfoot, 1960, "Transport Phenomena," John Wiley & Sons, Inc., pp 780.

Coantic, M., 1986, "A model of gas transfer across air-water interfaces with capillary waves. *J. Geophys. Res.* 91(C3), 3925-3943.

Liss, P., and Merlivat, L., 1986, "Air-sea gas exchange rates: Introduction and synthesis." In *Air-Sea Exchange of Gases and Particles.* D. Reidel, Dordrecht, 113. page

Rashidi K., and Banerjee, S., 1990, "The effect of boundary conditions and shear rate on streak formation and breakdown in turbulent channel flows." *Phys. Fluids* A2 1827.

Banner, M., and Philips, K., 1974, "On the incipient breaking of small scale waves" *J. Fluid Mech.* 65 647.

Kumar R., and Banerjee, S., 1998, "Development and application of a hierarchical system for digital particle image velocimetry to free- surface turbulence" *Phys. Fluids* 10 160.